

Models of crustal heating in accreting neutron stars

P. Haensel and J.L. Zdunik

N. Copernicus Astronomical Center, Polish Academy of Sciences, Bartycka 18, 00-716 Warszawa, Poland
haensel@camk.edu.pl, jlz@camk.edu.pl

Preprint online version: October 25, 2018

ABSTRACT

Aims. Heating associated with non-equilibrium nuclear reactions in accreting neutron-star crusts is reconsidered, taking into account suppression of neutrino losses demonstrated recently by Gupta et al. Two initial compositions of the nuclear burning ashes, $A_i = 56$ and $A_i = 106$, are considered. Dependence of the integrated crustal heating on uncertainties plaguing pycnonuclear reaction models is studied.

Methods. One-component plasma approximation is used, with compressible liquid-drop model of Mackie and Baym to describe nuclei. Evolution of a crust shell is followed from 10^8 g cm^{-3} to $10^{13.6} \text{ g cm}^{-3}$.

Results. The integrated heating in the outer crust agrees nicely with results of self-consistent multicomponent plasma simulations of Gupta et al.; their results fall between our curves obtained for $A_i = 56$ and $A_i = 106$. Total crustal heat per one accreted nucleon ranges between 1.5 MeV/nucleon to 1.9 MeV/nucleon for $A_i = 106$ and $A_i = 56$, respectively. The value of Q_{tot} depends weakly on the presence of pycnonuclear reactions at $10^{12} - 10^{13} \text{ g cm}^{-3}$. Remarkable insensitivity of Q_{tot} on the details of the distribution of nuclear processes in accreted crust is explained.

Key words. dense matter – equation of state – stars: neutron – stars: general – X-rays: bursts – X-ray: binaries – nuclear reactions

1. Introduction

Neutron star crust that is not in full thermodynamic equilibrium constitutes a reservoir of energy, which can then be released during star's evolution. Formation and structure of non-equilibrium neutron star crust was considered by many authors (Vartanyan & Ovakimova 1976; Bisnovatyi-Kogan & Chechetkin 1979; Sato 1979; Haensel & Zdunik 1990, 2003; Gupta et al. 2007). Such a state of the crust can be produced as a result of accretion of the matter onto a neutron star in a close low-mass X-ray binary, where the original crust built of a catalyzed matter could actually be replaced by a crust with composition strongly deviating from the nuclear equilibrium one.

Heating due to non-equilibrium nuclear processes taking place in the outer and inner crust of an accreting neutron star (deep crustal heating) was calculated by Haensel & Zdunik (1990) who used a simple model of one-component plasma, and assumed that the outer layers of the matter produced in the X-ray bursts consisted of pure ^{56}Fe . Another simplification used by Haensel & Zdunik (1990) consisted in assuming the ground-state - ground-state nuclear transitions due to the electron captures. Consequently, they maximized neutrino losses. Their calculated total deep crustal heating, produced mainly in the inner crust, was $Q_{\text{tot}} \sim 1.4 \text{ MeV}$ per one accreted nucleon. Haensel & Zdunik (2003) recalculated deep crustal heating for different initial composition of the outer layers, and obtained similar values of $Q_{\text{tot}} = 1.2 - 1.4 \text{ MeV/nucleon}$. Recently, heating of the outer crust of an accreting neutron star was studied by Gupta et al. (2007) who went beyond a simple model of Haensel & Zdunik (1990) and Haensel & Zdunik (2003). Namely, Gupta et al. (2007) considered a multicomponent plasma, a reaction network

of many nuclides, and included the contribution from the nuclear excited states. They found that electron captures in the outer crust lead mostly to the excited states of the daughter nuclei, which then deexcite heating the matter. Consequently, they found that the neutrino losses in the outer crust were negligible, which strongly increased the outer crust heating, compared to Haensel & Zdunik (2003) (by a factor of four). However, outer crust contributes only a small fraction of the Q_{tot} , and neutrino losses in the inner crust, where the bulk of Q_{tot} is produced are small, so that the original value of Haensel & Zdunik (1990), $Q_{\text{tot}} \sim 1.4 \text{ MeV/nucleon}$, remains quite a reasonable estimate (see Sect. 4 of the present paper).

The phenomenon of deep crustal heating appears to be relevant for the understanding of the thermal radiation observed in the soft X-ray transients (SXTs) in quiescence, when the accretion from a disk formed of plasma flowing from the low-mass companion star is switched off or strongly suppressed. Typically, the quiescent emission is much higher than the expected one for an old neutron star. It has been suggested that this is due to the fact that the interiors of neutron stars in SXTs are heated-up, during relatively short periods of accretion and bursting, by the non-equilibrium processes associated with nuclear reactions taking place in the deep layers of the crust (Brown et al. 1998). The deep crustal heating, combined with appropriate models of neutron-star atmosphere and interior, is used to explain observations of SXTs in quiescence. The luminosity in quiescence depends on the structure of neutron-star core, and particularly on the rate of neutrino cooling. This opened a new possibility of exploring the internal structure and equation of state of neutron stars via confrontation of theoretical models with observations of qui-

escent SXTs (see Colpi et al. 2001; Rutledge et al. 2002; Yakovlev et al. 2003, 2004; Levenfish & Haensel 2007).

Up to now, the crustal heating used in modeling SXTs was described using the model of Haensel & Zdunik (1990) (hereafter referred to as HZ90), updated and generalized by Haensel & Zdunik (2003) (hereafter referred to as HZ03). In these models, the heat was produced during the active (accretion) episodes, when the outer layer of neutron star was sinking in the neutron star interior under the weight of accreted matter. The very outer layer was assumed to be composed of the ashes of the X-ray bursts in the active epoch. For simplicity, those ashes were assumed to be a one-component plasma (^{56}Fe in HZ90 and ^{56}Fe and ^{106}Pd in HZ03). Under an increasing pressure, the composition of a sinking matter element was changing in a sequence of nuclear reactions: electron capture, neutron emission and absorption, and finally, at densities exceeding $10^{12} \text{ g cm}^{-3}$, also pycnonuclear fusion. As the nuclear processes were proceeding off-equilibrium, they were accompanied by the heat deposition in the crustal matter. The crustal heating was mostly supplied by the pycnonuclear fusion processes in the inner crust at $\rho = 10^{12} - 10^{13} \text{ g cm}^{-3}$. This seemingly crucial rôle of pycnonuclear reactions is embarrassing, because their rates are plagued by huge uncertainties. As shown by Yakovlev et al. (2006), the uncertainty in the calculated rate of pycnonuclear fusion of two ^{34}Ne nuclei, first pycnonuclear fusion in the inner crust as predicted by the HZ90 model, can be as large as seven (!) orders of magnitude. Therefore, there is a basic uncertainty about which pycnonuclear fusions do occur and at what densities. Fortunately, as we show in the present paper, this uncertainty does not affect significantly the value of Q_{tot} . However, it implies an ignorance concerning the distribution of heat sources in the inner crust. Possible observational constraints on the distribution of heat sources in the inner crust are discussed in Sect. 6.

In the present paper we redo the calculations of the crustal heating taking into account uncertainties in the pycnonuclear reaction rates as well as the suppression of the neutrino losses. We show that the uncertainties in the pycnonuclear reaction rates do not significantly affect the total heat release in the crust, while influencing of course the radial distribution of heat sources. We also show that the effect of excited states of daughter nuclei, while very important in the outer crust, does not lead to a significant increase of total crustal heating. Calculations are performed assuming two different initial nuclides produced in the X-ray bursts.

The plan of the paper is as follows. In Sect. 2 we briefly remind the scenario of the deep crustal heating, nuclear model used in simulations, and describe the relevant physical processes acting in the crust of an accreting neutron star. Results of selected simulations of the nuclear evolution of a matter element compressed from 10^8 g cm^{-3} to $10^{13.6} \text{ g cm}^{-3}$, are presented in the form of figures in Sect. 3 and tables in the Appendix. Total crustal heating is calculated in Sect. 4. In Sect. 5 we give an explanation of the weak model dependence of the total crustal heating (per one accreted nucleon). Our conclusions are presented in Sect. 6, where we also suggest an observational testing of the actual radial distribution of heat sources, which could be helpful in putting constraints on the deep crustal heating models.

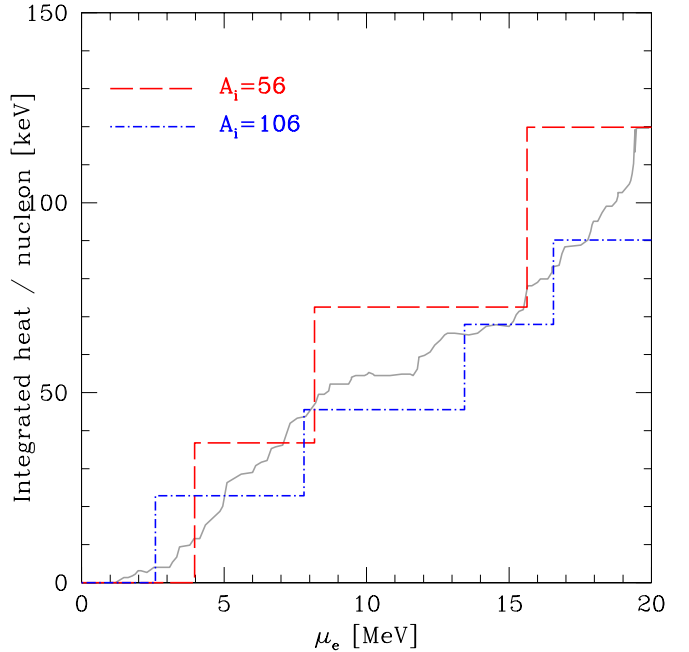
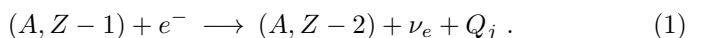
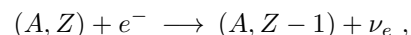


Fig. 1. (Color online) Integrated crustal heating per one accreted nucleon versus electron Fermi energy μ_e . The step-like curves were obtained using the HZ* model of the present paper, for two choices of an initial nuclide. The continuous curve was obtained by Gupta et al. (2007).

2. Non-equilibrium nuclear processes

2.1. Outer crust

In what follows we briefly describe the nuclear evolution scenario of HZ90 and HZ03, with correction implied by the results of Gupta et al. (2007). Under conditions prevailing in accreting neutron-star crust at $\rho > 10^8 \text{ g cm}^{-3}$ matter is strongly degenerate, and is relatively cold ($T < 10^8 \text{ K}$), so that thermonuclear processes involving charged particles can be assumed to be blocked by the Coulomb barrier. Consequently, the densities lower than the threshold for the pycnonuclear fusion (which is very uncertain, see Yakovlev et al. 2006, $\rho_{\text{pyc}} \sim 10^{12} - 10^{13} \text{ g cm}^{-3}$), the number of nuclei in an element of matter does not change during the compression resulting from the increasing weight of accreted matter. Let us remind, that we assume that only one nuclear species (A, Z) is present at each pressure (one component plasma). Due to the nucleon pairing, stable nuclei in dense matter have even $N = A - Z$ and Z (even-even nuclides). In the outer crust, in which free neutrons are absent, the electron captures which proceed in two steps,



lead to a systematic decrease of Z (and increase of $N = A - Z$) with increasing density. The first capture in Eq. (1) proceeds in a quasi-equilibrium manner, with a negligible energy release. It produces an odd-odd nucleus, which is strongly unstable in dense medium and captures a second electron in a non-equilibrium manner, with energy release Q_j , where j is the label of the non-equilibrium process.

2.2. Outer crust: comparison of HZ* model with Gupta et al. (2007)

In the original model of HZ90 electron captures were assumed to proceed from the ground state of the initial nucleus to the ground state of the daughter nucleus (GS-GS), and therefore most of the energy release was taken away by neutrinos (from 3/4 to 5/6 of Q_j , see Haensel & Zdunik 2003 for the discussion of this point). Very recently, an extensive, multicomponent self-consistent calculation of the nuclear evolution of an accreted matter element in the crust of a bursting neutron star was carried out by Gupta et al. (2007). As they have shown, electron captures to excited states (GS-ES) and subsequent de-excitation strongly reduce neutrino losses, so that nearly all released energy heats the crust matter. We therefore modified the original HZ model by neglecting neutrino losses accompanying electron captures: this model will be denoted as HZ*. Consider a version HZ* model, corresponding to specific choice of the initial mass number A_i , and denoted by a label (α). The integrated heat deposited in the crust in the layer with bottom density ρ can then be obtained as

$$Q^{(\alpha)}(\rho) = \sum_{j(\rho_j < \rho)} Q_j^{(\alpha)}. \quad (2)$$

In Fig. 1 we compare $Q(\mu_e)$, obtained for two HZ* models, with results of Gupta et al. (2007). We replaced ρ variable by the electron Fermi energy μ_e to facilitate the comparison. The curve of Gupta et al. (2007) lies between two extreme HZ* models; it has a very large number of small jumps. These two features reflect the multicomponent structure of crustal matter and large network of nuclear reactions in Gupta et al. (2007), with $50 \lesssim A_i \lesssim 110$. Generally, viewing the simplicity of the HZ* model, its agreement with multicomponent, self consistent calculations of Gupta et al. (2007), is very good.

2.3. Inner crust

Above the neutron-drip point ($\rho > \rho_{\text{ND}}$), electron captures trigger neutron emissions,

$$(A, Z) + e^- \longrightarrow (A, Z - 1) + \nu_e,$$

$$(A, Z - 1) + e^- \longrightarrow (A - k, Z - 2) + k n + \nu_e + Q_j. \quad (3)$$

Due to the electron captures, the value of Z decreases with increasing density. In consequence, the Coulomb barrier prohibiting the nucleus-nucleus reaction lowers. This effect, combined with the decrease of the mean distance between the neighboring nuclei, and a simultaneous increase of energy of the quantum zero-point vibrations around the nuclear lattice sites, opens a possibility of the pycnonuclear reactions. The pycnonuclear fusion timescale τ_{pyc} is a very sensitive function of Z . The chain of the reactions (3) leads to an abrupt decrease of τ_{pyc} typically by 7 to 10 orders of magnitude. Pycnonuclear fusion switches-on as soon as τ_{pyc} is smaller than the time of the travel of a piece of matter (due to the accretion) through the considered shell of mass $M_{\text{shell}}(N, Z)$, $\tau_{\text{acc}} \equiv M_{\text{shell}}/M$. The masses of the shells are of the order of $10^{-5} M_{\odot}$. As a result, in the inner crust the chain of reactions (3) in several cases is followed by the pycnonuclear reaction on a timescale much shorter than τ_{acc} .

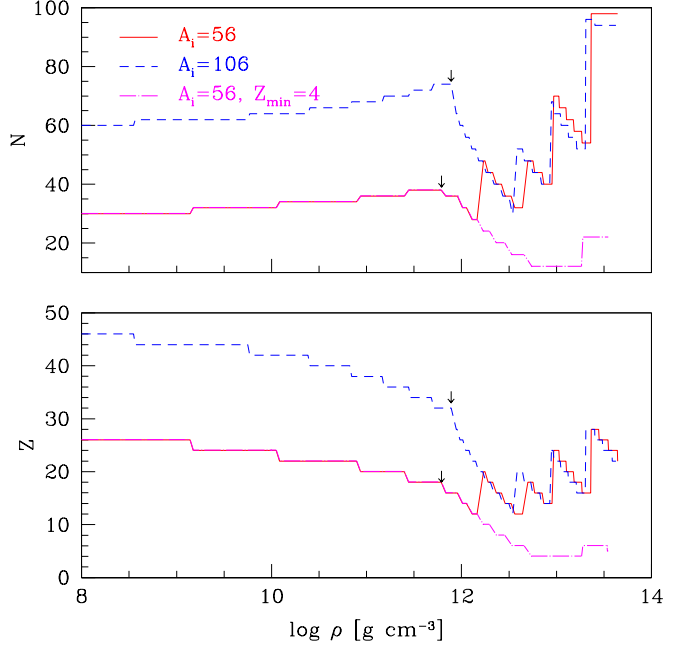


Fig. 2. (Color online) Z and N of nuclei, versus matter density in an accreting neutron-star crust, for different models of dense matter. Solid line: $A_i = 56$; dashed line: $A_i = 106$. Dash-dot line: continuation of $A_i = 56$ evolution but with pycnonuclear fusion blocked until $Z = Z_{\text{min}} = 4$. Each change of N and Z , which takes place at a constant pressure, is accompanied by a jump in density (see HZ90 for detailed discussion of this point). Small steep segments connect the top and the bottom density of thin reaction shell. Arrows indicate positions of the neutron drip point.

Denoting $Z' = Z - 2$, we have then

$$(A, Z') + (A, Z') \longrightarrow (2A, 2Z') + Q_{j,1},$$

$$(2A, 2Z') \longrightarrow (2A - k', 2Z') + k' n + Q_{j,2},$$

$$\dots \quad \dots \quad \dots \quad \dots + Q_{j,3}, \quad (4)$$

where “...” correspond to some not specified chain of the electron captures accompanied by neutron emissions. The total heat deposition in matter, resulting from a chain of reactions involving a pycnonuclear fusion, is $Q_j = Q_{j,1} + Q_{j,2} + Q_{j,3}$. In contrast to HZ03, and in accordance with Gupta et al. (2007), we neglect the neutrino losses accompanying the non equilibrium electron captures.

Our model of atomic nuclei is described in detail in HZ90. Using our nuclear-evolution code, we evolved an element of matter consisting initially of nuclei (A_i, Z_i) immersed in an electron gas, from $\rho_i = 10^8 \text{ g cm}^{-3}$ to $\rho = \rho_f > 5 \times 10^{13} \text{ g cm}^{-3}$. Our results for the composition and crustal heating are presented in the next section and in the Appendix.

3. Results of simulations: reactions, heating, compositions

The compositions of accreted neutron star crusts are shown in Fig. 2 and in tables in the Appendix. These results describe crusts built of accreted and processed matter up to

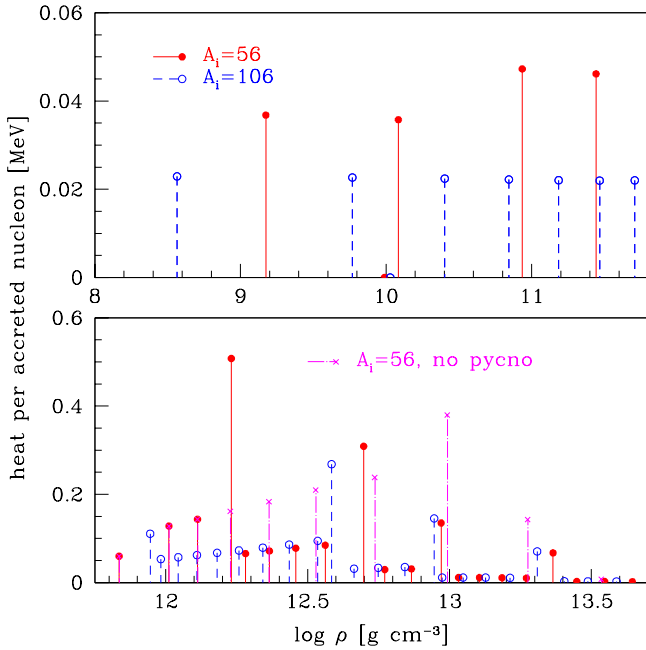


Fig. 3. (Color online) Heat sources in the outer (upper panel) and inner (crust) for three HZ* models. Vertical lines, positioned at the density at the bottom of the reaction shell, represent the heat per one accreted nucleon. Labels as in Table 2.

the density $5 \times 10^{13} \text{ g cm}^{-3}$. At a constant accretion rate $\dot{M} = \dot{M}_{-9} \times 10^{-9} M_{\odot}/\text{yr}$ this will take $\sim 10^6 \text{ yr}/\dot{M}_{-9}$. During that time, a shell of X-ray burst ashes will be compressed from $\sim 10^8 \text{ g cm}^{-3}$ to $\sim 10^{13} \text{ g cm}^{-3}$.

Two different compositions of X-ray bursts ashes at $\lesssim 10^8 \text{ g cm}^{-3}$ were assumed. In the first case, $A_i = 56$, $Z_i = 26$, like in HZ90. In the second scenario we followed HZ03, with $A_i = 106$, to imitate nuclear ashes obtained by Schatz et al. (2001). The value of $Z_i = 46$ stems then from the condition of beta equilibrium at $\rho = 10^8 \text{ g cm}^{-3}$. The density dependence of Z and $N = A - Z$ within the accreted crust is shown in Fig. 2. After pycnonuclear fusion region has been reached, both curves converged (as explained in HZ03, this results from A_i and Z_i in two scenarios differing by a factor of about two). Suppressing pycnonuclear fusion in the $A_i = 56$ case until $Z = Z_{\min} = 4$ yields the lowest curve.

In Fig. 3 we show the heat deposited in the matter, per one accreted nucleon, in the thin shells in which non-equilibrium nuclear processes are taking place. Actually, reactions proceed at a constant pressure, and there is a density jump within a thin “reaction shell”. The vertical lines whose height gives the heat deposited in matter are drawn at the density at the bottom of the reaction shell.

One notices a specific dependence of the number of heat sources and the heating power of a single source on assumed A_i . In the case of $A_i = 56$ the number of sources is smaller, and their heat-per-nucleon values Q_j are significantly larger, than for $A_i = 106$.

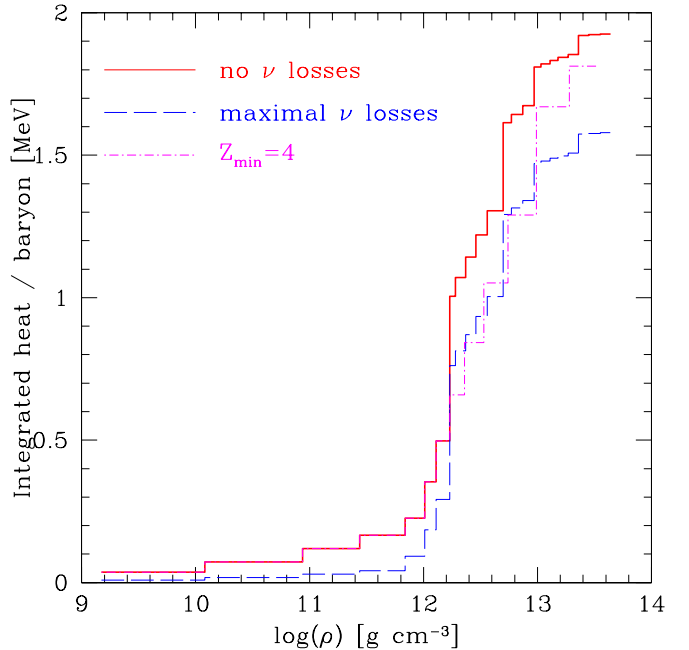


Fig. 4. (Color online) Integrated heat released in the crust, $Q(\rho)$ (per one accreted nucleon) versus ρ , assuming initial ashes of pure ^{56}Fe . Solid line: HZ* model of the present paper, with suppressed neutrino losses. Long dashes: GS-GS transitions in electron captures, with maximal neutrino losses. Dash-dot line: No neutrino losses, with pycnonuclear fusion blocked until $Z = Z_{\min} = 4$.

4. Integrated crustal heating

The quantity $Q^{(\alpha)}(\rho)$, for three specific models of compressional evolution, is plotted in Fig. 4. In the all three cases, we set $A_i = 56$ and $Z_i = 26$. For the first model, we neglect neutrino losses; its cumulated heat $Q^{(1)}$ is always the highest. The second model is used to visualize the important of excited states of the daughter nuclei in the electron captures. For this model we assumed that the nuclear transitions associated with electron captures are of the GS-GS type, which maximizes the neutrino losses. While the effect is dramatic for $\rho \lesssim 10^{12} \text{ g cm}^{-3}$, it implies only a 20% underestimate of Q above $10^{12.5} \text{ g cm}^{-3}$. But the most interesting is perhaps the effect of literally switching off of the pycnonuclear reactions, assumed in the third scenario. This was done by assuming that the pycnonuclear fusion is blocked till the nuclear charge goes down to $Z_{\min} = 4$. And yet, for $\rho_b > 10^{13} \text{ g cm}^{-3}$, $Q^{(3)}$ is very similar to that obtained in the first scenario, which was most advantageous as far as the crust heating was concerned. Namely, a missing pycnonuclear heating at $\rho \sim 10^{12} \text{ g cm}^{-3}$ is efficiently compensated by the electron captures accompanied by neutron emission within the density decade $10^{12} - 10^{13} \text{ g cm}^{-3}$. The values of Q saturate above $10^{13.6} \text{ g cm}^{-3}$, where 80% of nucleons are in neutron gas phase. All in all, for three scenarios with $A_i = 56$, the total deep crustal heat release is (1.6–1.9) MeV/nucleon. For $A_i = 106$, numbers are shifted downward by about 0.4 MeV/nucleon. The summary of our results for the total heat release is given in Table 1.

Table 1. Total crustal heating Q_{tot} for $A_i = 56$ and $A_i = 106$. First line: HZ* model of the present paper. Second line: old HZ03 model with maximal neutrino losses. Third and fourth lines: results obtained when neutrino losses are suppressed and pycnonuclear fusion is blocked down to $Z_{\text{min}} = 6$ and $Z_{\text{min}} = 4$, respectively.

$A_i = 56$			$A_i = 106$		
pycno	ν losses	Q_{tot}	pycno	ν losses	Q_{tot}
no blocking	none	1.93 MeV	no blocking	none	1.48 MeV
no blocking	maximal	1.58 MeV	no blocking	maximal	1.16 MeV
$Z_{\text{min}} = 6$	none	1.93 MeV	$Z_{\text{min}} = 6$	none	1.44 MeV
$Z_{\text{min}} = 4$	none	1.85 MeV	$Z_{\text{min}} = 4$	none	1.35 MeV

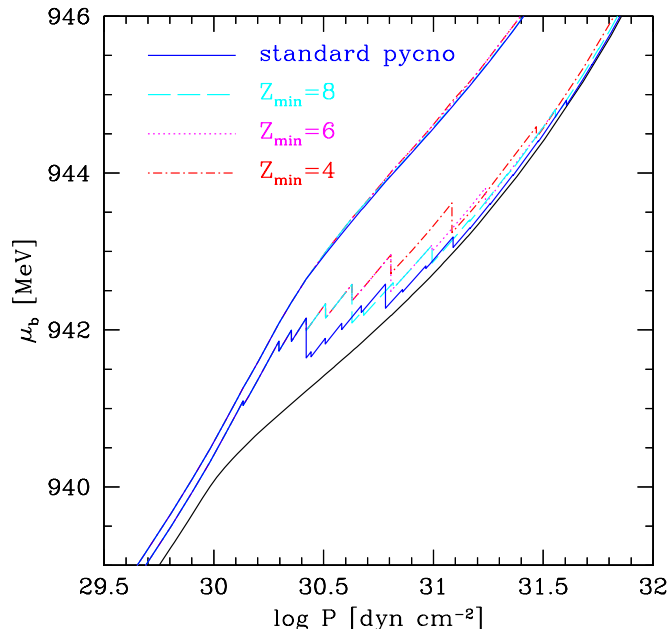


Fig. 5. (Color online) Baryon chemical potential $\mu_b(P)$ for different versions of blocking of pycnonuclear fusion. "Standard pycno" corresponds to HZ* model of the present paper, with $A_i = 56$. Three other curves correspond to pycnonuclear fusion suppressed until to $Z = Z_{\text{min}} = 8, 6, 4$, respectively. The upper continuous curves, which nearly coincide, are defined as $\bar{\mu}_b^{(\alpha)}(P) \equiv \mu_b^{(\alpha)}(P) + \sum_{j(P_j < P)} Q_j^{(\alpha)}$. Dependence of $\bar{\mu}_b^{(\alpha)}(P)$ on (α) is negligible, so that $\bar{\mu}_b^{(\alpha)}(P) \approx \bar{\mu}_b(P)$. The lowest smooth solid curve - cold catalyzed matter.

5. Constancy of the total heat release

Remarkably weak dependence of the total heat release in the crust, Q_{tot} , on the nuclear history of an element of matter undergoing compression from $\sim 10^8 \text{ g cm}^{-3}$ to $\sim 10^{13.6} \text{ g cm}^{-3}$, deserves an explanation. Let us therefore study the most relevant thermodynamic quantity, the Gibbs free energy per nucleon, which is the baryon chemical potential, μ_b . In the $T = 0$ approximation, $\mu_b(P) = [\mathcal{E}(P) + P]/n_b(P)$. Minimizing $\mu_b(P)$, at a fixed P , with respect to the independent thermodynamical variables (A , Z , mean free neutron density \bar{n}_n , mean baryon density n_b , size of the Wigner-Seitz cell, etc.), under the constraint of electric charge neutrality, $\bar{n}_p = \bar{n}_e$, we get the the ground state of the crust a given P . This state is called "cold cat-

alyzed" matter, and its baryon chemical $\mu_b^{(0)}(P)$ is represented in Fig. 5 by a solid black line. All other $\mu_b^{(\alpha)}(P)$ curves, showed in Fig. 5, display discontinuous drops due to non-equilibrium reactions included in a given evolutionary model (α) , and lie above the solid black one. This visualizes the fact that non-catalyzed matter is a reservoir of energy, released in non-equilibrium processes that push down matter closer to the absolute ground state. In spite of dramatic differences between different $\mu_b^{(\alpha)}(P)$ in the region where the bulk of non-equilibrium reactions and heating occur, $P = (10^{30} - 10^{31.5}) \text{ dyn cm}^{-2}$, these functions tend to the ground state one for $P \gtrsim 10^{32} \text{ dyn cm}^{-2}$. The general structure of different $\mu_b^{(\alpha)}(P)$ is similar. At same P , their continuous segments have nearly the same slope. What differs $\mu_b^{(\alpha)}(P)$ are discontinuous drops, by $Q_j^{(\alpha)}$, at reaction thresholds $P_j^{(\alpha)}$. The functions $\mu_b^{(\alpha)}(P)$ can therefore be expressed as

$$\mu_b^{(\alpha)}(P) \approx \bar{\mu}_b(P) - \sum_{j(P_j < P)} Q_j^{(\alpha)}, \quad (5)$$

where $\bar{\mu}_b(P)$ is a smooth function of P , independent of (α) (for explanation, see Fig. 5 and its caption). For $P > 10^{33.5} \text{ dyn cm}^{-2}$ the values of Q_j are negligibly small, and all $\mu_b^{(\alpha)}(P)$ become quite close to the ground state line. This implies, that the sum $\sum_j Q_j^{(\alpha)}$ has to be, to a rather good precision, *independent* of (α) .

6. Discussion and conclusion

In the present paper we reconsidered a model of deep crustal heating, formulated originally in (Haensel & Zdunik 1990, 2003). Following Gupta et al. (2007), we suppressed neutrino losses associated with electron captures. In this way we got the HZ* model of crustal heating that despite its simplicity (one component plasma) agrees nicely with results of self-consistent multi-component calculations of Gupta et al. (2007). Using the HZ* model we obtained the total crustal heating $Q_{\text{tot}} = 1.5 \text{ MeV}$ and 1.9 MeV/nucleon , for the initial ashes consisting of ^{106}Pd and ^{56}Fe , respectively. We studied the dependence of crustal heating on the location of the pycnonuclear fusion processes within the crust. It turned out that the total crustal heating (per one accreted nucleon) is quite insensitive to the depth at which pycnonuclear fusion occurs, with Q_{tot} varying at most by 0.2 MeV , and we presented an explanation of this feature.

Maximal neutrino losses, implied by the assumption of the ground-state - ground-state electron captures in

Haensel & Zdunik (1990) and Haensel & Zdunik (2003), led to a severe underestimate of the heating of the outer crust (Gupta et al. 2007). However, the outer crust gives a rather small contribution to the total crustal heating, Q_{tot} , and the underestimate of Q_{tot} is less than 25%. Composition of the initial ashes of the X-ray bursts can be more important for the value of Q_{tot} , as shown already in (Haensel & Zdunik 2003).

The insensitivity of Q_{tot} to the very uncertain rates of pycnoclear fusion means that this tremendous uncertainty, unlikely to be removed in spite of future theoretical efforts, does not affect the thermally equilibrated quiescent state of the SXTs. This may seem as good news. On the other hand, this means that the studies of SXTs in quiescence will not improve our knowledge of pycnonuclear fusion in dense plasma: this is bad news.

Fortunately, the situation changes with the access to observations of the thermal relaxation in SXTs after the accretion episode. This phenomenon cannot be observed in standard SXTs that remain in accreting state for days - weeks. Thermal relaxation can be observed only in so called persistent SXTs, characterized by accretion states lasting for years - decades. Such thermal relaxation, called initial cooling, has been observed in KS 1731-260 and MXB 1659-29 (Cackett et al. 2006). Let us focus on KS 1731-260. After 12.5 years of accretion and associated crustal heating, the crust of KS 1731-260 has become significantly hotter than the neutron star core. After accretion stopped, the heat cumulated in the crust diffused over the star, and the stellar surface cooled. The cooling curve of KS 1731-260 toward the quiescent state has been obtained by Cackett et al. (2006). This curve depends on the crust thermal conductivity, crust thickness, distribution of crustal heating sources, and on the neutrino cooling of neutron star core (Rutledge et al. 2002; Cackett et al. 2006).

There are two complementary aspects of observations of cooling of persistent SXTs. On the one hand, we need a theory to understand this phenomenon. On the other hand, observational data yield constraints on theoretical models. Very recently, simulations of thermal relaxation of KS 1731-260 were performed along these lines by Shternin et al. (2007). Increasing in number and precisions, observations of cooling curves in persistent SXTs will hopefully be a promising testing ground for the theories of deep crustal heating, including pycnonuclear fusion, and other physical processes in neutron stars.

Acknowledgements. We are very grateful to D.G. Yakovlev for a critical reading of the manuscript and for helpful remarks. This work was supported in part by the KBN grant 5 P03D 020 20 and the MNiSW grant N20300632/0450.

References

- Bildsten, L., & Chakrabarty, D. 2001, ApJ 557, 292
 Bisnovaty-Kogan, G.S., Chechetkin, V.M., 1979, Uspekhi Fiz. Nauk 127, 263 (English translation: Sov. Phys. Uspekhi 22, 89)
 Brown, E. F., Bildsten, L., & Rutledge, R. E. 1998, ApJ 504, L95
 Cackett E.M., Wijnands R., Linares M., Miller J.M., Homan J., Lewin W.H.G., 2006, MNRAS 372, 479
 Campana, S., Stella, L., Gastaldello, F., Mereghetti, S., Colpi, M., Israel, G. L., Burderi, L., Di Salvo, T., & Robba, R. N. 2002, ApJ 575, L15
 Colpi, M., Geppert, U., Page, D., & Possenti, A. 2001, ApJ 548, L175
 Chen, W., Shrader, C. R., & Livio, M. 1997, ApJ 491, 312
 Gupta, S., Brown E.F., Schatz, H., Möller, P., Kratz, K.-L., 2007, ApJ 662, 1188
 Haensel, P., & Zdunik, J. L., 1990, A&A, 227, 431
 Haensel, P., & Zdunik, J. L., 2003, A&A, 404, L33
 Levenfish, K.P., Haensel, P., 2007, Ap&SS, 308, 457
 Rutledge R.E., Bildsten L., Brown E.F., Pavlov G.G., Zavlin V.E., Ushomirsky G., 2002, ApJ, 580, 413
 Sato, K., 1979, Prog. Theor. Phys. 62, 957
 Schatz, H., Aprahamian, A., Barnard, V., et al., 2001, Phys. Rev. Lett. 86, 3471
 Schatz, H., Bildsten, L., Cumming, A., 2003, ApJ 583, L87
 Shternin, P.S., Yakovlev, D.G., Haensel, P., Potekhin, A.Y., 2007, MNRAS (submitted), arXiv:0708.0086 [astro-ph]
 Vartanyan, Yu.L., Ovakimova N.K., 1976, Soobtcheniya Byurakanskoi Observatorii 49, 87
 Yakovlev, D.G., Levenfish, K.P., Haensel, P., 2003, A&A 407, 265
 Yakovlev, D.G., Levenfish, K.P., Potekhin, A.Y., et al., 2004, A&A 417, 169
 Yakovlev, D.G., Gasques, L., Wiescher, M., 2006, MNRAS 371, 1322

Appendix A: Tables

Table A.1. Non-equilibrium processes in the crust of an accreting neutron stars assuming that the X-ray ashes consist of pure ^{106}Pd . P_j and ρ_j are pressure and density at which the reaction takes place. $\Delta\rho/\rho_j$ is relative density jump connected with reaction, Q_j is the heat deposited in the matter. X_n is the fraction of free neutrons among nucleons, and μ_e is the electron chemical potential, both in the layer just above the reaction surface.

P_j (dyn cm $^{-2}$)	ρ_j (g cm $^{-3}$)	reactions	X_n	$\Delta\rho/\rho_j$ %	μ_e (MeV)	Q_j (keV)
9.235×10^{25}	3.517×10^{08}	$^{106}\text{Pd} \rightarrow ^{106}\text{Ru} - 2e^- + 2\nu_e$	0	4.4	2.29	22.9
3.603×10^{27}	5.621×10^{09}	$^{106}\text{Ru} \rightarrow ^{106}\text{Mo} - 2e^- + 2\nu_e$	0	4.6	6.34	22.7
2.372×10^{28}	2.413×10^{10}	$^{106}\text{Mo} \rightarrow ^{106}\text{Zr} - 2e^- + 2\nu_e$	0	4.9	10.43	22.4
8.581×10^{28}	6.639×10^{10}	$^{106}\text{Zr} \rightarrow ^{106}\text{Sr} - 2e^- + 2\nu_e$	0	5.1	14.56	22.2
2.283×10^{29}	1.455×10^{11}	$^{106}\text{Sr} \rightarrow ^{106}\text{Kr} - 2e^- + 2\nu_e$	0	5.4	18.73	22.1
5.025×10^{29}	2.774×10^{11}	$^{106}\text{Kr} \rightarrow ^{106}\text{Se} - 2e^- + 2\nu_e$	0	5.7	22.91	22.0
9.713×10^{29}	4.811×10^{11}	$^{106}\text{Se} \rightarrow ^{106}\text{Ge} - 2e^- + 2\nu_e$	0	6.1	27.08	22.0
1.703×10^{30}	7.785×10^{11}	$^{106}\text{Ge} \rightarrow ^{92}\text{Ni} + 14n - 4e^- + 4\nu_e$	0.13	13.2	31.22	110.8
1.748×10^{30}	8.989×10^{11}	$^{92}\text{Ni} \rightarrow ^{86}\text{Fe} + 6n - 2e^- + 2\nu_e$	0.19	6.9	31.33	53.2
1.924×10^{30}	1.032×10^{12}	$^{86}\text{Fe} \rightarrow ^{80}\text{Cr} + 6n - 2e^- + 2\nu_e$	0.25	7.3	31.02	57.5
2.135×10^{30}	1.197×10^{12}	$^{80}\text{Cr} \rightarrow ^{74}\text{Ti} + 6n - 2e^- + 2\nu_e$	0.30	7.7	32.76	62.1
2.394×10^{30}	1.403×10^{12}	$^{74}\text{Ti} \rightarrow ^{68}\text{Ca} + 6n - 2e^- + 2\nu_e$	0.36	8.1	33.57	67.2
2.720×10^{30}	1.668×10^{12}	$^{68}\text{Ca} \rightarrow ^{62}\text{Ar} + 6n - 2e^- + 2\nu_e$	0.42	8.5	34.45	72.9
3.145×10^{30}	2.016×10^{12}	$^{62}\text{Ar} \rightarrow ^{56}\text{S} + 6n - 2e^- + 2\nu_e$	0.47	9.0	35.44	79.2
3.723×10^{30}	2.488×10^{12}	$^{56}\text{S} \rightarrow ^{50}\text{Si} + 6n - 2e^- + 2\nu_e$	0.53	9.4	36.57	86.0
4.549×10^{30}	3.153×10^{12}	$^{50}\text{Si} \rightarrow ^{42}\text{Mg} + 8n - 2e^- + 2\nu_e$	0.61	8.8	37.86	94.5
4.624×10^{30}	3.472×10^{12}	$^{42}\text{Mg} \rightarrow ^{36}\text{Ne} + 6n - 2e^- + 2\nu_e$				
		$^{36}\text{Ne} + ^{36}\text{Ne} \rightarrow ^{72}\text{Ca}$	0.66	10.6	37.13	268.2
5.584×10^{30}	4.399×10^{12}	$^{72}\text{Ca} \rightarrow ^{66}\text{Ar} + 6n - 2e^- + 2\nu_e$	0.69	4.8	37.56	31.6
6.883×10^{30}	5.355×10^{12}	$^{66}\text{Ar} \rightarrow ^{60}\text{S} + 6n - 2e^- + 2\nu_e$	0.72	4.7	39.00	33.5
8.749×10^{30}	6.655×10^{12}	$^{60}\text{S} \rightarrow ^{54}\text{Si} + 6n - 2e^- + 2\nu_e$	0.75	4.6	40.33	35.2
1.157×10^{31}	8.487×10^{12}	$^{54}\text{Si} \rightarrow ^{46}\text{Mg} + 8n - 2e^- + 2\nu_e$				
		$^{46}\text{Mg} + ^{46}\text{Mg} \rightarrow ^{92}\text{Cr}$	0.79	4.0	41.84	145.3
1.234×10^{31}	9.242×10^{12}	$^{92}\text{Cr} \rightarrow ^{86}\text{Ti} + 6n - 2e^- + 2\nu_e$	0.80	2.0	40.88	11.4
1.528×10^{31}	1.096×10^{13}	$^{86}\text{Ti} \rightarrow ^{80}\text{Ca} + 6n - 2e^- + 2\nu_e$	0.82	1.9	42.04	11.4
1.933×10^{31}	1.317×10^{13}	$^{80}\text{Ca} \rightarrow ^{74}\text{Ar} + 6n - 2e^- + 2\nu_e$	0.83	1.8	43.31	11.2
2.510×10^{31}	1.609×10^{13}	$^{74}\text{Ar} \rightarrow ^{68}\text{S} + 6n - 2e^- + 2\nu_e$	0.85	1.7	44.71	10.6
3.363×10^{31}	2.003×10^{13}	$^{68}\text{S} \rightarrow ^{62}\text{Si} + 6n - 2e^- + 2\nu_e$				
		$^{62}\text{Si} + ^{62}\text{Si} \rightarrow ^{124}\text{Ni}$	0.86	1.7	46.26	70.5
4.588×10^{31}	2.520×10^{13}	$^{124}\text{Ni} \rightarrow ^{120}\text{Fe} + 4n - 2e^- + 2\nu_e$	0.87	0.8	47.78	3.0
5.994×10^{31}	3.044×10^{13}	$^{120}\text{Fe} \rightarrow ^{118}\text{Cr} + 2n - 2e^- + 2\nu_e$	0.88	0.9	49.65	2.7
8.408×10^{31}	3.844×10^{13}	$^{118}\text{Cr} \rightarrow ^{116}\text{Ti} + 2n - 2e^- + 2\nu_e$	0.88	0.8	52.28	2.5

Table A.2. Nuclear processes and released heat in the inner crust, assuming initial ashes of pure ^{106}Pd (i.e. as in Table A.1) but suppressing pycnonuclear fusion until $Z = Z_{\min} = 4$. Only the lines different than those in the Table A.1 are presented. The network of reactions below pressure $P = 4.624 \times 10^{30}$ dyn cm $^{-2}$ is the same as in the Table A.1.

P_j (dyn cm $^{-2}$)	ρ_j (g cm $^{-3}$)	reactions	X_n	$\Delta\rho/\rho_j$ %	μ_e (MeV)	Q_j (keV)
4.624×10^{30}	3.472×10^{12}	$^{42}\text{Mg} \rightarrow ^{36}\text{Ne} + 6n - 2e^- + 2\nu_e$	0.66	9.9	37.13	76.0
6.253×10^{30}	4.745×10^{12}	$^{36}\text{Ne} \rightarrow ^{30}\text{O} + 6n - 2e^- + 2\nu_e$	0.72	9.9	38.79	84.2
9.323×10^{30}	6.937×10^{12}	$^{30}\text{O} \rightarrow ^{24}\text{C} + 6n - 2e^- + 2\nu_e$	0.77	9.4	40.89	91.8
1.615×10^{31}	1.119×10^{12}	$^{24}\text{C} \rightarrow ^{18}\text{Be} + 6n - 2e^- + 2\nu_e$	0.84	9.2	43.59	94.4
3.500×10^{31}	2.071×10^{13}	$^{18}\text{Be} \rightarrow ^{15}\text{Li} + 3n - 1e^- + 1\nu_e$				
		$^{15}\text{Li} + ^{15}\text{Li} \rightarrow ^{28}\text{C} + 2n$	0.88	2.3	46.78	152.8
6.339×10^{31}	3.166×10^{13}	$^{28}\text{C} \rightarrow ^{27}\text{B} + 1n - 1e^- + 1\nu_e$	0.89	1.9	48.98	8.7

Table A.3. Non-equilibrium processes in the crust of an accreting neutron stars assuming that the X-ray ashes consist of pure ^{56}Fe . P_j and ρ_j are pressure and density at which the reaction takes place. $\Delta\rho/\rho_j$ is relative density jump connected with reaction, Q_j is the heat deposited in the matter. X_n is the fraction of free neutrons among nucleons, and μ_e is the electron chemical potential, both in the layer just above the reaction surface.

P (dyn cm $^{-2}$)	ρ (g cm $^{-3}$)	Process	X_n	$\Delta\rho/\rho$	μ_e	q (keV)
7.23×10^{26}	1.49×10^9	$^{56}\text{Fe} \rightarrow ^{56}\text{Cr} - 2e^- + 2\nu_e$	0	0.08	4.08	40.7
9.57×10^{27}	1.11×10^{10}	$^{56}\text{Cr} \rightarrow ^{56}\text{Ti} - 2e^- + 2\nu_e$	0	0.09	8.18	35.8
1.15×10^{29}	7.85×10^{10}	$^{56}\text{Ti} \rightarrow ^{56}\text{Ca} - 2e^- + 2\nu_e$	0	0.10	15.64	47.3
4.75×10^{29}	2.50×10^{11}	$^{56}\text{Ca} \rightarrow ^{56}\text{Ar} - 2e^- + 2\nu_e$	0	0.11	22.48	46.1
1.36×10^{30}	6.11×10^{11}	$^{56}\text{Ar} \rightarrow ^{52}\text{S} + 4n - 2e^- + 2\nu_e$	0	0.12	29.38	59.8
1.980×10^{30}	9.075×10^{11}	$^{52}\text{S} \rightarrow ^{46}\text{Si} + 6n - 2e^- + 2\nu_e$	0.07	0.13	32.27	128.0
2.253×10^{30}	1.131×10^{12}	$^{46}\text{Si} \rightarrow ^{40}\text{Mg} + 6n - 2e^- + 2\nu_e$	0.18	0.14	32.22	143.5
2.637×10^{30}	1.455×10^{12}	$^{40}\text{Mg} \rightarrow ^{34}\text{Ne} + 6n - 2e^- + 2\nu_e$				
		$^{34}\text{Ne} + ^{34}\text{Ne} \rightarrow ^{68}\text{Ca}$	0.39	0.17	34.34	507.9
2.771×10^{30}	1.766×10^{12}	$^{68}\text{Ca} \rightarrow ^{62}\text{Ar} + 6n - 2e^- + 2\nu_e$	0.45	0.8	34.47	65.8
3.216×10^{30}	2.134×10^{12}	$^{62}\text{Ar} \rightarrow ^{56}\text{S} + 6n - 2e^- + 2\nu_e$	0.45	0.09	35.47	71.6
3.825×10^{30}	2.634×10^{12}	$^{56}\text{S} \rightarrow ^{50}\text{Si} + 6n - 2e^- + 2\nu_e$	0.50	0.09	36.59	77.9
4.699×10^{30}	3.338×10^{12}	$^{50}\text{Si} \rightarrow ^{44}\text{Mg} + 6n - 2e^- + 2\nu_e$	0.55	0.09	37.89	84.6
6.043×10^{30}	4.379×10^{12}	$^{44}\text{Mg} \rightarrow ^{36}\text{Ne} + 8n - 2e^- + 2\nu_e$				
		$^{36}\text{Ne} + ^{36}\text{Ne} \rightarrow ^{72}\text{Ca}$				
		$^{72}\text{Ca} \rightarrow ^{66}\text{Ar} + 6n - 2e^- + 2\nu_e$	0.61	0.14	39.41	308.8
7.233×10^{30}	5.839×10^{12}	$^{66}\text{Ar} \rightarrow ^{60}\text{S} + 6n - 2e^- + 2\nu_e$	0.70	0.04	39.01	29.5
9.238×10^{30}	7.041×10^{12}	$^{60}\text{S} \rightarrow ^{54}\text{Si} + 6n - 2e^- + 2\nu_e$	0.73	0.04	40.34	31.0
1.228×10^{31}	8.980×10^{12}	$^{54}\text{Si} \rightarrow ^{48}\text{Mg} + 6n - 2e^- + 2\nu_e$				
		$^{48}\text{Mg} + ^{48}\text{Mg} \rightarrow ^{96}\text{Cr}$				
		$^{96}\text{Cr} \rightarrow ^{94}\text{Cr} + 2n$	0.80	0.04	41.86	135.1
1.463×10^{31}	1.057×10^{13}	$^{94}\text{Cr} \rightarrow ^{88}\text{Ti} + 6n - 2e^- + 2\nu_e$	0.81	0.02	41.99	11.5
1.816×10^{31}	1.254×10^{13}	$^{88}\text{Ti} \rightarrow ^{82}\text{Ca} + 6n - 2e^- + 2\nu_e$	0.82	0.02	43.18	11.3
2.304×10^{31}	1.506×10^{13}	$^{82}\text{Ca} \rightarrow ^{76}\text{Ar} + 6n - 2e^- + 2\nu_e$	0.84	0.02	44.48	10.9
2.998×10^{31}	1.838×10^{13}	$^{76}\text{Ar} \rightarrow ^{70}\text{S} + 6n - 2e^- + 2\nu_e$	0.85	0.02	45.91	10.0
4.028×10^{31}	2.287×10^{13}	$^{70}\text{S} \rightarrow ^{64}\text{Si} + 6n - 2e^- + 2\nu_e$				
		$^{64}\text{Si} + ^{64}\text{Si} \rightarrow ^{128}\text{Ni}$				
		$^{128}\text{Ni} \rightarrow ^{126}\text{Ni} + 2n$	0.87	0.01	47.48	67.3
5.278×10^{31}	2.784×10^{13}	$^{126}\text{Ni} \rightarrow ^{124}\text{Fe} + 2n - 2e^- + 2\nu_e$	0.88	0.01	48.50	2.5
7.311×10^{31}	3.493×10^{13}	$^{124}\text{Fe} \rightarrow ^{122}\text{Cr} + 2n - 2e^- + 2\nu_e$	0.89	0.01	51.05	2.4

Table A.4. Nuclear processes and released heat in the inner crust, assuming initial ashes of pure ^{56}Fe (i.e. as in Table A.3) but suppressing pycnonuclear fusion until $Z = Z_{\text{min}} = 4$. Only the lines different than those in the Table A.3 are presented. The network of reactions below pressure $P = 2.637 \times 10^{30}$ dyn cm $^{-2}$ is the same as in the Table A.3.

P (dyn cm $^{-2}$)	ρ (g cm $^{-3}$)	reactions	X_n	$\Delta\rho/\rho$ %	μ_e (MeV)	q (keV)
2.637×10^{30}	1.455×10^{12}	$^{40}\text{Mg} \rightarrow ^{34}\text{Ne} + 6n - 2e^- + 2\nu_e$	0.40	16.0	34.45	161.4
3.227×10^{30}	1.961×10^{12}	$^{34}\text{Ne} \rightarrow ^{28}\text{O} + 6n - 2e^- + 2\nu_e$	0.50	17.9	35.71	183.4
4.254×10^{30}	2.831×10^{12}	$^{28}\text{O} \rightarrow ^{22}\text{C} + 6n - 2e^- + 2\nu_e$	0.61	19.4	37.49	209.8
6.392×10^{30}	4.541×10^{12}	$^{22}\text{C} \rightarrow ^{16}\text{Be} + 6n - 2e^- + 2\nu_e$	0.72	20.0	39.89	238.2
1.216×10^{31}	8.617×10^{12}	$^{16}\text{Be} \rightarrow ^{13}\text{Li} + 4n - 1e^- + 1\nu_e$				
		$^{13}\text{Li} + ^{13}\text{Li} \rightarrow ^{26}\text{C}$				
		$^{26}\text{C} \rightarrow ^{24}\text{C} + 2n$	0.79	7.5	43.18	331.2
1.727×10^{31}	1.186×10^{13}	$^{24}\text{C} \rightarrow ^{18}\text{Be} + 6n - 2e^- + 2\nu_e$	0.85	7.4	43.64	84.1
3.798×10^{31}	2.200×10^{12}	$^{18}\text{Be} \rightarrow ^{17}\text{Li} + 1n - 1e^- + 1\nu_e$				
		$^{17}\text{Li} + ^{17}\text{Li} \rightarrow ^{34}\text{C}$				
		$^{34}\text{C} \rightarrow ^{30}\text{C} + 4n$	0.88	0.028	46.86	142.0